Phase separation in highly charged confined ionic solutions

Rémi Joubaud, Olivier Bernard, Lorenzo Contento, Alexandre Ern, Benjamin Rotenberg, Pierre Turq

PHASE SEPARATION IN HIGHLY CHARGED CONFINED IONIC SOLUTIONS

R. JOUBAUD[1,2,3], O. BERNARD[4,5], L. CONTENTO[6], A. ERN[2], B. ROTENBERG[4,5], AND P. TURQ[5,4]

Abstract. We study phase separation in ionic solutions confined by solid objects carrying surface charges. Within the framework of Density Functional Theory, the Helmholtz free energy of the ionic solution is minimized under canonical constraints on the ionic densities fixing their mean value while ensuring global electroneutrality. The free energy splits into a bulk and an electrostatic contribution. The bulk contribution, which includes non-ideal terms accounting for long-range electrostatic and short-range steric correlations between ions, is evaluated with the Mean Spherical Approximation and the Local Density Approximation. The Primitive Model is considered with counter- and co-ions having the same diameter. The electrostatic contribution treats the interactions between the ions and the solid object at the mean-field level through the solution of a suitable Poisson problem. The numerical methodology hinges on a regularization of the free energy and a finite element discretization of the Euler-Lagrange conditions of the constrained minimization problem on adaptively refined meshes as the regularization parameter approaches zero. Results are presented for the one-dimensional double-layer configuration and a multi-dimensional periodic network of charged circular inclusions. The main results are the formation of a condensed phase near the charge solid surface screening most of the surface charge, the stark contrast with predictions using the Poisson–Boltzmann theory, and the fact that co-ion densities are higher in the condensed phase as well. An extension of the methodology to the case where ions do not carry opposite charges is also presented.

1. Introduction

Charged solutes and charged interfaces are encountered in numerous natural and technological contexts, largely due to the ability of water to solvate ions and to screen their electrostatic interactions by its high dielectric permittivity. In this paper, we are interested in the study of ionic solutions interacting with (or confined by) solid objects carrying a surface charge (clay rocks, colloids, DNA, or electrodes, to name only a few examples). Multi-valent ions and electrolytes near such highly charged objects may depart significantly from the ideal behavior of infinitely diluted solutions. We are particularly interested in studying confinements at the nanometric scale and the possible separation of the solution into a condensed phase close to the charged object and a dilute phase away from it.

In bulk situations, the non-ideal behavior of ionic solutions arises mainly from two types of effects, which both play a larger role as the ionic concentration increases: long-range electrostatic interactions and short-range excluded volume effects. By treating the former at the mean-field level and ignoring the latter, the pioneering work of Debye and Hückel (DH) [1] identified screening by counter-ions as a fundamental mechanism for non-ideality. The DH theory is valid at low concentrations and high temperature. For more concentrated solutions, further progress has been accomplished within the framework of the primitive models of charged hard spheres in a continuous solvent characterized by its dielectric constant,

whereby structural and thermodynamic properties are predicted using integral equation theories, such as the Mean Spherical Approximation (MSA) [2, 3, 4, 5]. Liquid-vapor transition and criticality in bulk ionic solutions have been extensively investigated over the past decades. The properties of the liquid-vapor interface have been studied using a density-functional theory (DFT) within the restricted primitive model (RPM) in which the ions are modelled as equi-sized spheres carrying opposite charges [6]. Moreover, by combining Bjerrum's ion pairing concept [7] with the MSA or the DH theory through the law of mass action, better descriptions of the critical point and of the liquid-vapor coexistence curve have been obtained [8, 9, 10, 11, 12].

In the case of ionic solutions in contact with charged solid surfaces, e.g., in confined geometries, electrostatic interactions also control the structure and the phase behavior of the solution [13, 14, 15]. In some cases, such as clay minerals, cement, ion exchange membranes or lipid bilayers, the counter-ions compensating the charge of the surface may even be the only ions present in the confined fluid, resulting in a situation similar to the one-component plasma (see [16] for a review and [17] for a discussion closer to the present setting). The starting point for the description of confined ionic solutions is the Poisson–Boltzmann (PB) theory [18, 19, 20]. The PB theory ignores correlations between ions, and no phase transition exists within this approach. For highly charged surfaces or multi-valent ions, a large fraction of the counter-ions appears condensed near the charged surface, as suggested by Stern to generalize the Gouy-Chapman description of charged surfaces. The remaining ions then feel a much weaker effective charge, which can be described within the PB theory. Nevertheless, the determination of the fraction of condensed ions and the corresponding renormalized charge is not straightforward; results in this direction can be found in [21]. Various approaches have been proposed to incorporate correlations neglected in the PB theory. In the particular case where counter-ions are the only ions present, a perturbative correction to the PB theory has been established [22]. Correlations for confined ions can also be included in integral theories, e.g., within the Anisotropic Hypernetted Chain approximation [23, 24]. Furthermore, the so-called "Strong Coupling" theory allows one to investigate regimes where the interaction with the charged surface is stronger than that between ions [25, 26, 27, 28] and to explain the origin of the attraction between like-charged surfaces observed under certain conditions [28, 29]. Another successful development for the description of the inhomogeneous primitive model is the use of DFT, which determines structural and thermodynamic properties of an inhomogeneous fluid from a Helmholtz free energy and its functional dependence on the local ionic densities [30, 31, 32, 33, 34, 35, 36, 37]. Finally, Molecular Dynamics and Monte Carlo simulations have been used to study the properties of bulk and confined electrolytes, described either within the primitive model or with an explicit molecular solvent, thus providing a more realistic description of these complex systems [38, 39, 40, 41, 42]. Although such simulations remain computationally intensive, and may not be needed to elucidate the phase transition behavior of confined ionic solutions, they can serve as a basis for multi-scale strategies in which continuous approaches, such as the one presented here, are parametrized for a given system using molecular simulations [17].

The present study of confined ionic solutions is based on DFT, where the Helmholtz free energy of the system depends on the ionic densities and splits into a bulk and an electrostatic contribution. The former incorporates the ideal and non-ideal effects in the bulk solution regardless of the presence of the charged solid object. The electrostatic contribution accounts for the electrostatic potential due to the presence of the solid object carrying surface charges and is evaluated consistently with the ionic densities as the solution of a suitable Poisson

problem. Thus, the interactions between the ions and the charged solid surface are treated at the mean-field level. Our main objective is to investigate numerically phase separation in confined ionic solutions for simple (one-dimensional) and more complex (multi-dimensional) geometric setups. Non-ideal effects in the bulk free energy account for correlations between ions, including both long-range electrostatic and short-range steric contributions. These correlations are evaluated with the MSA and the Local Density Approximation (LDA) [43]. More elaborate models for non-ideality can be incorporated in further steps. These can include a more elaborate treatment of excluded volume effects near the solid surface (which can lead to attraction between like-charged surfaces), improvements in the description of electrostatic correlations near the critical point, and a more precise treatment of ion-solvent interactions especially for multi-valent ions and very small confinements.

The material is organized as follows. In Sect. 2 we detail the free energy of the confined ionic solution describing its bulk and electrostatic contributions. In particular, the screening length evaluated with the MSA depends on a non-dimensional parameter which can be interpreted as a reduced temperature. The starting point is the minimization of the free energy functional. While grand-canonical constraints are often considered in the literature, we focus here on canonical constraints on the ionic densities fixing their mean value in the fluid domain while ensuring global electroneutrality. We are interested in the regime where the reduced temperature falls below the critical one. In this situation, the above constrained minimization problem becomes ill-posed. Our approach consists in enforcing additionally that the ionic densities take values in the subset of the state space where the bulk free energy functional coincides with its convex hull. This condition typically leads to the appearance in the fluid domain of an interface separating a condensed and a dilute phase. In Sect. 3, we present the numerical methodology to solve the constrained minimization problem. We relax the constraint on the values of the ionic densities by considering a regularization of the free energy functional obtained by adding a least-squares penalty on the gradient of the ionic densities weighted by a positive parameter η. While a physically-based parameter η can be considered in some models, this quantity merely plays herein the role of a numerical parameter. The Euler–Lagrange equations associated with the regularized free energy functional are solved in mixed form by introducing the electrostatic potential as an auxiliary variable. These equations are discretized using finite elements on adaptively refined meshes near the interface, and the resulting system of nonlinear algebraic equations is solved iteratively using a Newton–Raphson algorithm. In Sect. 4 and 5, we discuss our results for confined ionic solutions containing only compensating counter-ions and both counter- and co-ions, respectively. We consider the double-layer configuration of two parallel charged plates confining the ionic solution and also a two-dimensional periodic network of circular objects carrying a surface charge to demonstrate the capabilities of the present methodology in multi-dimensional setups. Finally, in Sect. 6, we summarize our main findings and discuss further work.

2. Free energy of confined ionic solutions

We consider ionic solutions in the presence of solid objects with surface charges. Two typical situations are either that of an ionic solution in a periodic setting with elementary cells containing a charged inclusion or that of an ionic solution confined by charged walls. These two situations are illustrated in Figure 1. The length scale associated with the confinement is denoted by L_* and is typically of the order of a nanometer. The domain occupied by the ionic solution is denoted by Ω, and the domain occupied by the solid object is denoted by Ω_{S}.

To be specific, we assume that the solid object carries negative charges with surface density $-\Sigma_{\mathrm{S}}$ ($\Sigma_{\mathrm{S}} > 0$) on its boundary $\partial\Omega_{\mathrm{S}}$.

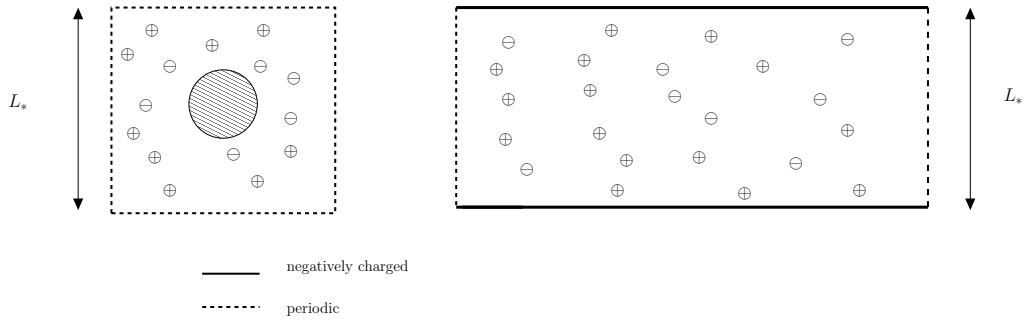

FIGURE 1. Geometric setting: elementary cell with charged inclusion (left); channel with charged walls (right).

For simplicity, we consider at most two dissolved ionic species, a counter-ion (cation) and a co-ion (anion). Within the primitive model retained herein, ions are modelled as equi-sized spheres of diameter σ. However, we do not necessarily assume that ions carry opposite charges (as they do in the RPM). The valences of the ionic species are denoted by $Z_{\pm}$, and the case where $Z_+ + Z_- = 0$ is referred to as symmetric electrolyte. The ionic solution is described by the ionic (number) densities $\rho := (\rho_+, \rho_-)$ in the fluid domain Ω, while the solvent enters the model only by means of its relative dielectric permittivity. In what follows, the mean-value of the ionic densities is prescribed in the form

$$\langle \rho_{\pm} \rangle_{\Omega} = \rho_{\pm}^{\mathrm{mean}}, \tag{1}$$

where $\langle \cdot \rangle_{\Omega}$ denotes the mean-value of a function in the fluid domain Ω. The prescribed nonnegative quantities $\rho_{\pm}^{\mathrm{mean}}$ must satisfy the global electroneutrality condition

$$\sum_{i=\pm} Z_i \rho_i^{\mathrm{mean}} = \frac{1}{e|\Omega|} \int_{\partial\Omega_{\mathrm{S}}} \Sigma_{\mathrm{S}}, \tag{2}$$

where e is the elementary charge. A simple way of ensuring the global electroneutrality condition (2) is to choose a nonnegative density of added salt, ρ^{salt}, and to set

$$\rho_+^{\mathrm{mean}} = \rho_+^{\Sigma_{\mathrm{S}}} + \rho^{\mathrm{salt}}, \qquad \rho_-^{\mathrm{mean}} = -(Z_+/Z_-)\rho^{\mathrm{salt}}, \tag{3}$$

where $\rho_+^{\Sigma_{\mathrm{S}}} := (Z_+ e|\Omega|)^{-1} \int_{\partial\Omega_{\mathrm{S}}} \Sigma_{\mathrm{S}}$. In the vanishing limit of added salt, $\rho^{\mathrm{salt}} \to 0^+$, we obtain an ionic solution consisting only of compensating counter-ions.

The free energy functional of the ionic solution takes the form

$$\mathcal{F}(\rho) = \mathcal{F}_{\mathrm{bulk}}(\rho) + \mathcal{F}_{\mathrm{elst}}(\rho). \tag{4}$$

The bulk free energy functional $\mathcal{F}_{\mathrm{bulk}}$ accounts for the ideal and non-ideal behavior in the bulk solution regardless of the presence of the charged solid object, while the electrostatic free energy functional $\mathcal{F}_{\mathrm{elst}}$ accounts for the electrostatic potential. The functionals $\mathcal{F}_{\mathrm{bulk}}$ and $\mathcal{F}_{\mathrm{elst}}$ are detailed in Sect. 2.1 and 2.2, respectively. The equilibrium state of the ionic solution is determined by minimizing $\mathcal{F}$ under the canonical constraint (1). We are particularly interested in the case where the functional $\mathcal{F}_{\mathrm{bulk}}$ is not convex in ρ, as further discussed in Sect. 2.3.

2.1. **Bulk free energy functional.** Within the LDA, the bulk free energy is obtained by integrating over the fluid domain Ω the bulk free energy density f, so that

$$\mathcal{F}_{\mathrm{bulk}}(\rho) = \int_\Omega f(\rho). \tag{5}$$

The bulk free energy density splits into an ideal part f_{id} and a non-ideal part f_{corr} in the form

$$f(\rho) = f_{\mathrm{id}}(\rho) + f_{\mathrm{corr}}(\rho), \qquad f_{\mathrm{corr}}(\rho) = f_{\mathrm{Coul}}(\rho) + f_{\mathrm{HS}}(\rho), \tag{6}$$

where f_{corr} accounts for Coulomb electrostatic interactions (through f_{Coul}) and hard-sphere steric exclusion effects (through f_{HS}). The ideal part reads

$$f_{\mathrm{id}}(\rho) = \frac{1}{\beta\sigma^3}\sum_{i=\pm}\hat{\rho}_i(\log(\hat{\rho}_i) - 1), \tag{7}$$

with non-dimensional ionic densities $\hat{\rho}_\pm := \sigma^3\rho_\pm$, while $\beta := (k_{\mathrm{B}}T)^{-1}$ where k_{B} is the Boltzmann constant and T the temperature. The Coulomb contribution is chosen to be of the MSA form [2, 3, 4, 5]

$$f_{\mathrm{Coul}}(\rho) = -\frac{1}{4\pi\beta\sigma^3}\left(\hat{\rho}_\alpha - 4\Gamma_{\mathrm{MSA}}(\hat{\rho}_\alpha)^2 - \frac{16}{3}\Gamma_{\mathrm{MSA}}(\hat{\rho}_\alpha)^3\right), \tag{8}$$

with $\hat{\rho}_\alpha := (\hat{\rho}_+/\alpha_+) + (\hat{\rho}_-/\alpha_-)$ and the non-dimensional parameters

$$\alpha_\pm := \frac{\sigma}{4\pi L_{\mathrm{B}} Z_\pm^2}. \tag{9}$$

Here, L_{B} stands for the Bjerrum length given by $L_{\mathrm{B}} := (4\pi\varepsilon)^{-1}\beta e^2$ where $\varepsilon = \varepsilon_0\varepsilon_{\mathrm{r}}$ with ε_0 the vacuum dielectric permittivity and ε_{r} the solvent relative dielectric permittivity. The parameters $\alpha_\pm$ are related to non-dimensional temperatures $T_\pm^*$ such that

$$T_\pm^* := 4\pi\alpha_\pm = k_{\mathrm{B}}T\frac{\sigma(4\pi\varepsilon)}{Z_\pm^2 e^2}, \tag{10}$$

while the inverse Debye length κ is such that

$$\kappa\sigma = \hat{\rho}_\alpha^{1/2}. \tag{11}$$

The (non-dimensional) screening parameter Γ_{MSA} is given by

$$\Gamma_{\mathrm{MSA}}(\hat{\rho}_\alpha) = \frac{1}{2}\left(\left(2\hat{\rho}_\alpha^{1/2} + 1\right)^{1/2} - 1\right). \tag{12}$$

Moreover, the hard-sphere contribution, which hinges on the Carnahan–Starling (CS) expression, is given by

$$f_{\mathrm{HS}}(\rho) = \begin{cases} -\dfrac{6}{\pi\beta\sigma^3}\left(\dfrac{\xi(\hat{\rho}_{\mathrm{tot}})^2\left(3\xi(\hat{\rho}_{\mathrm{tot}}) - 4\right)}{\left(1 - \xi(\hat{\rho}_{\mathrm{tot}})\right)^2}\right), & \xi(\hat{\rho}_{\mathrm{tot}}) < 1, \\ +\infty, & \xi(\hat{\rho}_{\mathrm{tot}}) \geq 1, \end{cases} \tag{13}$$

with reduced total ionic density $\hat{\rho}_{\mathrm{tot}} := \hat{\rho}_+ + \hat{\rho}_-$ and packing number $\xi(\hat{\rho}_{\mathrm{tot}}) := \frac{1}{6}\pi\hat{\rho}_{\mathrm{tot}}$. In the dilute limit of low ionic densities leads to the linearized hard-sphere contribution (CS1) in the form

$$f_{\mathrm{HS}}(\rho) = \frac{1}{\beta\sigma^3}\frac{24}{\pi}\xi(\hat{\rho}_{\mathrm{tot}})^2. \tag{14}$$

A simplification occurs for symmetric electrolytes ($Z_+ + Z_- = 0$), since, in this case, $\alpha_+ = \alpha_- := \alpha$ and $T_+^* = T_-^* := T^*$. Moreover, $\hat{\rho}_\alpha = \alpha^{-1}\hat{\rho}_{\mathrm{tot}}$. As a result, $f_{\mathrm{corr}}(\rho)$ only depends on $\hat{\rho}_{\mathrm{tot}}$ and its properties can be described in terms of the reduced temperature T^*.

2.2. **Electrostatic free energy functional.** The electrostatic potential is evaluated consistently with the ionic densities by solving a Poisson problem in the fluid domain Ω with source term given by the charge density $q(\rho) = \sum_{i=\pm} Z_i e \rho_i$ and a Neumann boundary condition accounting for the surface charge carried by the solid object on $\partial\Omega_{\mathrm{S}}$. Specifically, the electrostatic potential $\psi(\rho)$ solves

$$\begin{cases} -\varepsilon\Delta\psi(\rho) = q(\rho) \quad \text{in } \Omega, \\ -\varepsilon\nabla\psi(\rho)\cdot\boldsymbol{n} = \Sigma_{\mathrm{S}} \quad \text{on } \partial\Omega_{\mathrm{S}}, \\ \psi(\rho) \text{ periodic on } \partial\Omega \setminus \partial\Omega_{\mathrm{S}}, \\ \langle\psi(\rho)\rangle_\Omega = 0, \end{cases} \tag{15}$$

where $\boldsymbol{n}$ denotes the unit outward normal to Ω. The global electroneutrality condition (2) ensures that problem (15) admits a solution, and uniqueness of the solution results from the zero mean condition on $\psi(\rho)$. The electrostatic free energy functional is given by

$$\mathcal{F}_{\mathrm{elst}}(\rho) = \frac{1}{2}\left(\int_\Omega q(\rho)\psi(\rho) - \int_{\partial\Omega_{\mathrm{S}}} \Sigma_{\mathrm{S}}\psi(\rho)\right) = \frac{\varepsilon}{2}\int_\Omega |\nabla\psi(\rho)|^2\,, \tag{16}$$

the second equality being a direct consequence of (15) and integration by parts.

2.3. **Minimizing the free energy functional.** We aim at determining the equilibrium state of the ionic solution by minimizing the free energy functional $\mathcal{F}$ under the canonical constraint (1). A sufficient well-posedness condition for this problem hinges on the strict convexity of the bulk free energy density f with respect to the ionic densities ρ. This situation, which has been studied mathematically in [44] (using the linearized hard-sphere term (14)), is encountered when the reduced temperatures $T_\pm^*$ are high enough (typically, above the critical temperature) so that the non-convexity of the Coulomb interaction term f_{Coul} is compensated by the convexity of the ideal and hard-sphere terms f_{id} and f_{HS}.

In the present work, we are interested in the regime where at least one of the reduced temperatures $T_\pm^*$ is low enough (typically, below the critical temperature) so that the bulk free energy density f is no longer convex with respect to the ionic densities ρ. In the case of bulk ionic solutions, this regime is known to lead to liquid-vapor transition. In such solutions, the ionic densities satisfy the local electroneutrality condition $\sum_{i=\pm} Z_i e\rho_i = 0$, so that the bulk free energy density f can be analyzed as a univariate function of, e.g., the total density $\hat{\rho}_{\mathrm{tot}}$. The binodal points of f can be evaluated using the double-tangent construction (also known as Maxwell's equal-area rule). These points determine the liquid-vapor coexistence curves in the phase diagram of the bulk ionic solution. An example is presented in Figure 2 for a bulk symmetric electrolyte (so that a single reduced temperature T^* is considered). The critical temperature and (total) density are respectively $T^*_{\mathrm{crit}} \approx 0.0787$ and $\hat{\rho}_{\mathrm{tot,crit}} \approx 0.0147$ for CS1 (using (14)) and $T^*_{\mathrm{crit}} \approx 0.0785$ and $\hat{\rho}_{\mathrm{tot,crit}} \approx 0.0145$ for CS (using (13), in agreement with the result previously derived in [6]. Differences between CS and CS1 expectedly appear for high values of the total density.

For confined ionic solutions, the situation becomes more intricate. The presence of the charged solid object induces gradients in the ionic densities and, thereby, departures from local electroneutrality. As a result, the whole state space $\mathcal{K} := \{\rho \in \mathbb{R}^2; \rho_\pm \geq 0; \xi(\hat{\rho}) < 1\}$

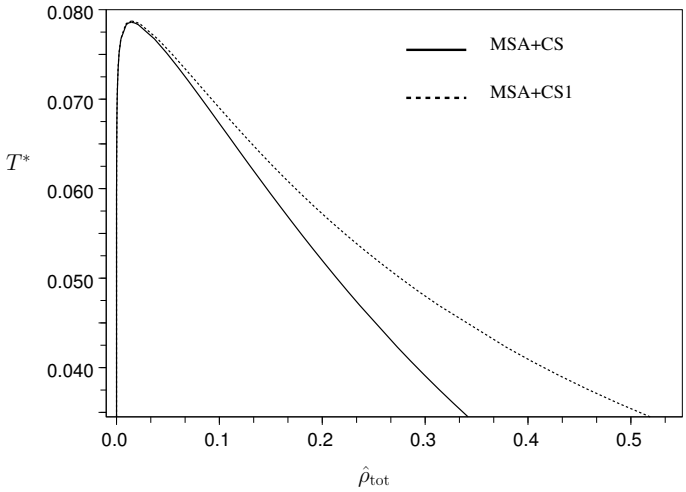

FIGURE 2. Phase diagram for a bulk symmetric electrolyte. For each T^* below the critical temperature, the curves provide the two binodal values for the reduced total density.

can potentially be explored by the ionic densities at different points in the fluid domain Ω. Hence, the bulk free energy density has to be considered as a fully bivariate function of its two arguments $\rho_\pm$. Letting f^{**} be the convex hull of f, we introduce the subset

$$\mathcal{K}^{**} = \{\rho \in \mathcal{K}; f(\rho) = f^{**}(\rho)\}. \tag{17}$$

Our key idea in the confined case is then to supplement the constrained minimization problem of $\mathcal{F}$ with the additional constraint that, everywhere in the fluid domain Ω, the ionic densities take values in the subset $\mathcal{K}^{**}$. Therefore, our model problem can be stated as follows:

$$\begin{cases} \rho \text{ minimizes } \mathcal{F}(\rho) \text{ defined by (4)}, \\ \rho \text{ satisfies the canonical constraint (1)}, \\ \text{For all } x \in \Omega,\ \rho(x) \text{ takes values in } \mathcal{K}^{**} \text{ defined by (17)}. \end{cases} \tag{18}$$

The model problem (18) can be easily adapted to the case where there are only compensating counter-ions by setting $\rho_- = 0$ and considering ρ_+ as the only independent variable so that the relevant bulk free energy density is $f_+(\rho_+) := f(\rho_+, 0)$. The state space then reduces to $\mathcal{K}_+ := \{\rho_+ \in \mathbb{R}; \rho_+ \geq 0; \xi(\hat{\rho}_+) < 1\}$, and the subset $\mathcal{K}^{**}$ is replaced by the subset $\mathcal{K}_+^{**} = \{\rho_+ \in \mathcal{K}_+; f_+(\rho_+) = f_+^{**}(\rho_+)\}$ where f_+^{**} is the convex hull of the univariate function f_+. We observe that $\mathcal{K}_+^{**}$ is a subset of $\mathbb{R}$, whereas $\mathcal{K}^{**}$ is a subset of $\mathbb{R}^2$. The determination of the subset $\mathcal{K}_+^{**}$ is straightforward from Figure 2. Namely, given a reduced temperature $T^* = T_+^*$ below the critical temperature, the binodal points of f_+ are deduced from the liquid-vapor coexistence curves in which $\hat{\rho}_{\rm tot}$ is replaced by $\hat{\rho}_+$. Denoting by $\hat{\rho}_+^\flat$ and $\hat{\rho}_+^\sharp$ these two points yields $\mathcal{K}_+^{**} = [0, \hat{\rho}_+^\flat] \cup [\hat{\rho}_+^\sharp, 6/\pi]$ (up to rescaling by σ^3), the first interval corresponding to the dilute (gas) phase and the second one to the condensed (liquid) phase. In the bivariate case, the determination of the subset $\mathcal{K}^{**}$ is further discussed in Sect. 5.

3. Numerical method

The mathematical analysis of the constrained minimization problem (18) goes beyond the present scope. Assuming well-posedness, the aim of this section is to devise a numerical method to approximate its solution.

3.1. **Regularization and Euler–Lagrange conditions.** There is an extensive bibliography concerning the mathematical and numerical study of phase separation in other settings than confined electrolytes. In general, the functional used in such phase-field theory is a double-well potential inducing a partition of the state space into two phases. Most of the studies have been performed in bulk situations where the state variable (here, the ionic densities) is constant in each phase. The key idea is to regularize the problem by minimizing a regularized functional where a least-squares penalty on the gradient of the state variable is added to the double-well potential. For the mathematical analysis, we refer, e.g., to the seminal work in [45]; further references and links to Γ-convergence can be found in [46]. Other recent results concerning the study of the Ohta–Kawasaki model (modelling diblock copolymer systems) are relevant here owing to the similarity of the mathematical problem. We also mention the mathematical and numerical works in [47, 48], and, more recently, [49] where a nonlocal operator accounting for Coulomb interaction is added.

In the present setting, we handle the constraint that the ionic densities take values in the set $\mathcal{K}^{**}$ by introducing a regularization of the free energy functional in the form

$$\mathcal{F}_\eta(\rho) := \mathcal{F}(\rho) + \frac{\eta^2 L_*^5}{\beta} \sum_{i=\pm} \int_\Omega \frac{1}{2} |\nabla \rho_i|^2, \tag{19}$$

with non-dimensional regularization parameter $\eta > 0$. The constrained minimization problem (18) is then replaced by seeking ionic densities ρ_η such that

$$\begin{cases} \rho_\eta \text{ minimizes } \mathcal{F}_\eta(\rho_\eta) \text{ defined by (19)}, \\ \rho_\eta \text{ satisfies the canonical constraint (1)}. \end{cases} \tag{20}$$

Solving (20) with a fixed positive value of the regularization parameter η typically leads to a diffuse interface between the two phases, that is, the set $\mathcal{I} := \{x \in \Omega; \rho(x) \notin \mathcal{K}^{**}\}$ has positive measure. The sharp interface approximation $\eta \to 0^+$ leads to two distinct phases occupying the whole fluid domain Ω while the measure of $\mathcal{I}$ tends to zero; an illustration is presented in Sect. 3.3 below. In the present study, the regularization parameter η plays the role of a (very) small numerical parameter. From a physical viewpoint, a diffuse interface is more appropriate based on a certain length scale. One interesting approach is to resort to a Weighted Density Approximation (WDA) instead of the LDA whereby a coarse-grained density obtained by convolution of the local density is used in the free energy; see, e.g., [37].

We consider the Euler–Lagrange equations associated with the constrained minimization problem (20). These equations are formulated in mixed form by introducing as an additional unknown the electrostatic potential $\psi_\eta := \psi(\rho_\eta)$ solving (15) with datum $q(\rho_\eta)$ in Ω. The constraints to be taken into account are the canonical constraint (1) on the ionic densities ρ_η and the fact that ψ_η has zero mean value in Ω. In view of finite element discretization, we write the Euler–Lagrange equations in variational form using test functions. Thus, we seek

ionic densities ρ_η, electrostatic potential ψ_η, and real numbers λ_η et $\mu_\pm^{\mathrm{bulk}}$ such that

$$\left\{\begin{array}{l} \displaystyle\int_\Omega \varepsilon\nabla\psi_\eta\cdot\nabla\varphi + \lambda_\eta\langle\varphi\rangle_\Omega = \int_\Omega q(\rho_\eta)\varphi - \int_{\partial\Omega_{\mathrm{S}}}\Sigma_{\mathrm{S}}\varphi, \\ \displaystyle\eta^2 L_*^5\beta^{-1}\int_\Omega \nabla\rho_{\eta,\pm}\cdot\nabla v_\pm + \int_\Omega \mu_\pm^{\mathrm{el}}(\rho_\eta,\psi_\eta)v_\pm = \mu_\pm^{\mathrm{bulk}}|\Omega|\langle v\rangle_\Omega, \\ r\langle\psi_\eta\rangle_\Omega = 0, \qquad s_\pm(\langle\rho_{\eta,\pm}\rangle_\Omega - \rho_\pm^{\mathrm{bulk}}) = 0, \end{array}\right. \tag{21}$$

for all test functions φ and $v_\pm$ and for all real numbers r and $s_\pm$. The electro-chemical potential $\mu_\pm^{\mathrm{el}}(\rho_\eta,\psi_\eta)$ is such that

$$\mu_\pm^{\mathrm{el}}(\rho_\eta,\psi_\eta) := \mu_\pm(\rho_\eta) + Z_\pm e\psi_\eta, \tag{22}$$

with chemical potential

$$\mu_\pm(\rho_\eta) := \partial_{\rho_\pm} f(\rho_\eta). \tag{23}$$

For $\eta = 0$, the second equation in (21) expresses that the electro-chemical potentials are constant in Ω (with constant value equal to $\mu_\pm^{\mathrm{bulk}}$). We also observe that in the diffuse interface case ($\eta > 0$), the regularization term weakly enforces an inconsistent homogeneous Neumann condition on the ionic densities at the boundary $\partial\Omega_{\mathrm{S}}$, namely $\nabla\rho_{\eta,\pm}\cdot\boldsymbol{n} = 0$; this condition disappears in the sharp interface approximation as $\eta\to 0^+$.

3.2. **Finite element discretization and nonlinear algebraic solver.** The Euler–Lagrange equations (21) are discretized using finite elements. Once a mesh of the fluid domain Ω has been selected, the electrostatic potential and the ionic densities are approximated using continuous, piecewise affine functions over that mesh. This leads to a large system of nonlinear algebraic equations which is solved iteratively using a Newton–Raphson algorithm.

When the bulk free energy density f is not convex, the chemical potentials $\mu_\pm$ defined by (23) are non-monotone functions of the ionic densities, and this, in turn, poses difficulties to achieve convergence of the Newton–Raphson iterations (21). To overcome these difficulties, we introduce an additional regularization in that the chemical potentials are evaluated using the convex hull f^{**} of the bulk free energy density, that is, we use

$$\mu_\pm^{\mathrm{reg}}(\rho_\eta) := \partial_{\rho_\pm} f^{**}(\rho_\eta) \tag{24}$$

in place of $\mu_\pm(\rho_\eta)$ to evaluate the electro-chemical potential in the second equation of (21). By construction, the functions $\mu_\pm^{\mathrm{reg}}(\rho_\eta)$ are monotone in $\rho_{\eta,\pm}$, respectively. Using $\mu_\pm^{\mathrm{reg}}(\rho_\eta)$ in place of $\mu_\pm(\rho_\eta)$ modifies the solution in the diffusive interface case ($\eta > 0$), but the same solution is expected to be attained in the sharp interface approximation as $\eta\to 0^+$ since, in this case, the ionic densities essentially take values in $\mathcal{K}^{**}$ where f and f^{**} coincide.

Each Newton–Raphson iteration consists in assembling a linear system whose solution provides an update for the discrete solution vector. By linearity, at each iteration, the electrostatic potential is evaluated consistently with the ionic densities, and the constraints on the mean value of both the electrostatic potential and the ionic densities are satisfied. In practice, it is important to apply a clipping to the update vector to avoid that the ionic densities take negative values or values such that the packing number exceeds unity. If such a clipping is applied to some components of the update vector, the other components are rescaled in such a way that the canonical constraint (1) is still verified. The convergence of the Newton–Raphson algorithm is monitored by checking the Euclidean norm of the discrete residual vector and that of the update vector at each iteration. Typically, 40 to 50 iterations

can be necessary to achieve convergence for the systems investigated in the following sections. The above-mentioned clipping is usually needed only at a few iterations. More details on the algorithmic aspects can be found in [50].

3.3. **Sharp interface approximation.** This approximation entails decreasing progressively the value of the numerical parameter η. When a certain value for η is considered, the initial guess for the Newton–Raphson algorithm is the converged discrete solution for the previously considered value of η. It is essential to refine the mesh in the vicinity of the interface as it becomes sharper. Such a refinement is performed adaptively based on the converged discrete solution for the previously considered value of η; we refer to [50] for more details and examples.

To illustrate the sharp interface approximation, we present in Figure 3 concentration profiles (in mol.L^{-1}) in the double-layer configuration (consisting of two parallel charged plates separated by a distance L_*, see Figure 1) with only compensating counter-ions. Profiles are presented for various decreasing values of the parameter η as a function of the distance to the wall and up to the symmetry plane; a zoom close to the interface is included. The physical parameters (corresponding to water at room temperature, for which $L_{\mathrm{B}} = 7.10$ Å) are $L_* = 1$ nm, $\Sigma_{\mathrm{S}} = 0.1$ C.m^{-2}, $Z_+ = 3$, $\sigma = 4.5$ Å, and $T^* = 0.0704$ (below the critical value $T^*_{\mathrm{crit}} = 0.0785$). We observe how the interface separating the two phases is captured as $\eta \to 0^+$. The left and right limits of the concentration profile at the interface correspond, respectively, to the binodal points $\hat{\rho}^\sharp_+$ and $\hat{\rho}^\flat_+$ of the bulk free energy density. Away from the interface, the concentration profiles appear to coincide almost exactly, independently of the parameter η. Moreover, the above-mentioned boundary layer near the charged wall caused by the slight inconsistency in the least-squares penalty appears to be indeed negligible.

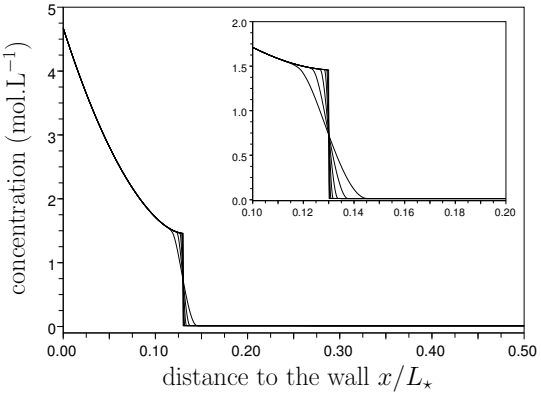

FIGURE 3. Sharp interface approximation for the double-layer configuration ($\eta \to 0^+$). Concentration profiles from the charged wall to the symmetry plane for various decreasing values of η. The insert is a zoom in the vicinity of the interface.

4. Results without added salt

In this section, we focus on ionic solutions consisting only of a dissolved counter-ion, so that $\rho^{\mathrm{salt}} = 0$ in (3) and ρ_- is identically zero in Ω. We recall that in this case, $\mathcal{K}^{**}_+ = [0, \hat{\rho}^\flat_+] \cup [\hat{\rho}^\sharp_+, 6/\pi]$ (up to rescaling by σ^3) where the binodal points $\hat{\rho}^\flat_+$ and $\hat{\rho}^\sharp_+$ are determined from Figure 2 at a given reduced temperature T^*. We first consider the double-layer configuration.

By symmetry, the problem can be posed on the half-interval $\Omega = [0, L_*/2]$. We set $L_* = 1$ nm. We consider a medium-sized divalent counter-ion ($Z_+ = 2$, $\sigma = 2.2$ Å, and $T^* = 0.07746$ (slightly) below $T^*_{\rm crit} = 0.0785$) and a larger trivalent counter-ion ($Z_+ = 3$, $\sigma = 4.5$ Å, and $T^* = 0.07042$ again below $T^*_{\rm crit}$). In the divalent case, we set $\Sigma_{\rm S} = 0.5$ or 1.0 C.m^{-2}, which correspond, respectively, to the canonical constraint $\rho_+^{\rm mean} = 5.191$ mol.L^{-1} or 10.38 mol.L^{-1} (in this second case, the packing number is $\xi(\rho_+^{\rm mean}) = 0.067$). In the trivalent case, we set $\Sigma_{\rm S} = 0.3$ or 0.5 C.m^{-2}, which correspond, respectively, to the canonical constraint $\rho_+^{\rm mean} = 2.077$ mol.L^{-1} or 3.461 mol.L^{-1} (in this second case, $\xi(\rho_+^{\rm mean}) = 0.190$).

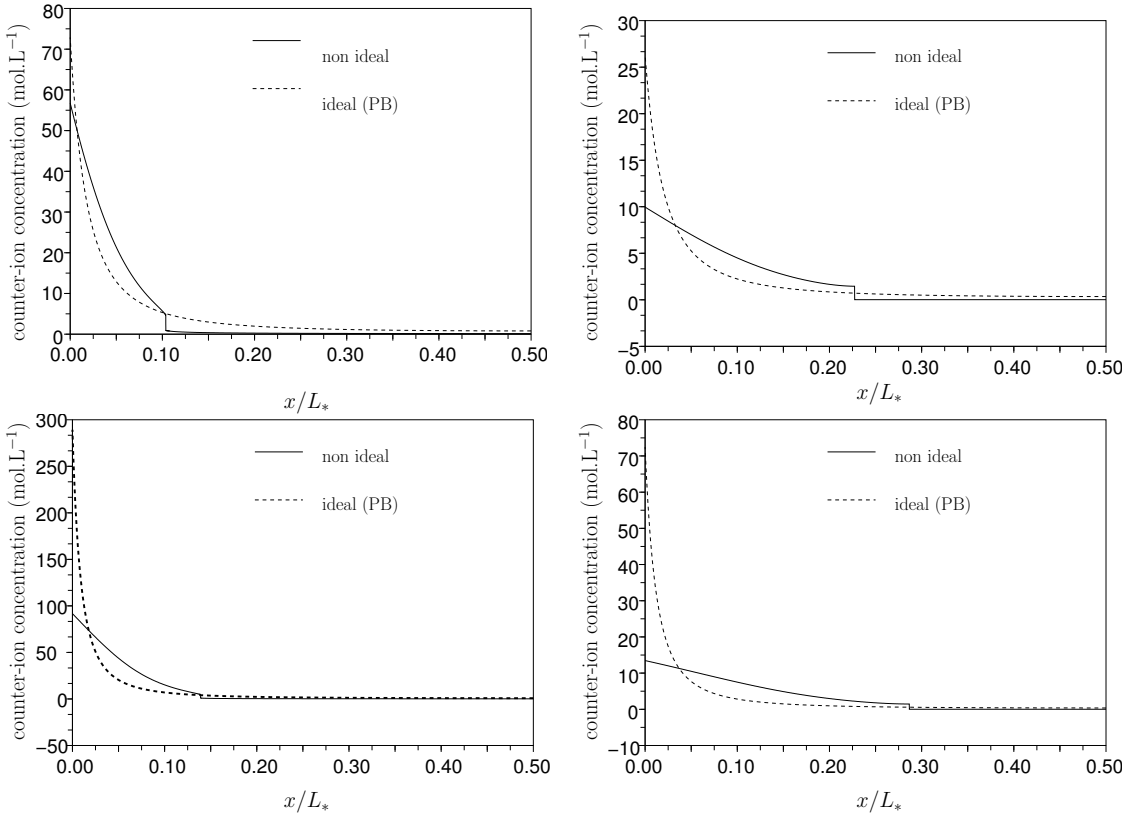

FIGURE 4. Double-layer configuration with compensating counter-ion. Concentration profiles from the charged wall to the symmetry plane. Left column: divalent counter-ions with $\Sigma_S = 0.5$ C.m^{-2} (top) and $\Sigma_S = 1$ C.m^{-2} (bottom). Right column: trivalent counter-ions with $\Sigma_S = 0.3$ C.m^{-2} (top) and $\Sigma_S = 0.5$ C.m^{-2} (bottom). Dashed lines correspond to the profiles obtained using the PB theory.

Figure 4 presents counter-ion concentration profiles (in mol.L^{-1}) as a function of the reduced distance to the charged wall. We observe the separation of the solution into two phases, a condensed phase close to the charged wall where most of the counter-ions concentrate and screen out the surface charge, and a dilute phase away from the charged wall where the counter-ion concentration is very small. These profiles are in stark contrast with the predictions of the PB theory (shown with dashed lines) since the PB theory does not predict phase

separation. Another interesting consequence of our results is that more than 90% (and in some cases up to 99%) of the surface charge carried by the confining walls is screened out by the counter-ions in the condensed phase, so that the remaining counter-ions in the dilute phase feel a much weaker effective charge which can be determined quantitatively. Figure 5 presents the distance of the phase interface to the charged wall as a function of the surface charge density for divalent counter-ions. While the order of magnitude of this distance is roughly equal to the ion radius, variations by changing Σ_S are sizable. The increase in the distance is a consequence of correlations between ions, whose concentration at the surface increases with surface charge density. Instead, as indicated by further simulations, this distance is not very sensitive to the wall separation distance L_* when the latter is in the range of a nanometer.

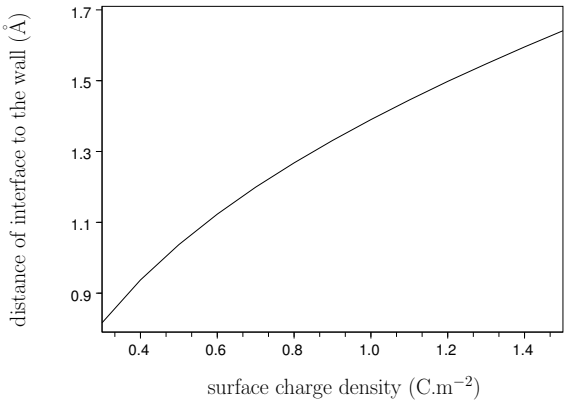

FIGURE 5. Distance of the phase interface to the charged wall as a function of the surface charge density for divalent counter-ions.

Another significant difference with respect to the PB theory concerns the total pressure in the system, which, for the present double-layer configuration, can be evaluated by computing the osmotic pressure at the symmetry plane. The osmotic pressure depends on the counter-ion density ρ_+ (recall that $\rho_- \equiv 0$ here) in the form

$$p_{\mathrm{osm}}(\rho_+) = \rho_+ \mu_+(\rho_+) - f(\rho_+). \tag{25}$$

Owing to the double-tangent construction of the convex hull, the osmotic pressure is continuous across the interface separating the two phases. At the symmetry plane, the osmotic pressure takes very small values, which are at least two orders of magnitude lower than those predicted by the PB theory. Such an important difference results from the fact that the condensed phase (which results from non-ideal behavior) screens out most of the surface charges carried by the walls. However, despite these substantial quantitative differences, the present model for non-ideality still leads to positive osmotic pressures, albeit very small. Negative pressures cannot be predicted with the present model since ρ_+ takes values in the set where f coincides with its convex hull f^{**}. This implies that p_{osm} can also be evaluated as $p_{\mathrm{osm}}(\rho_+) = \rho_+ \partial_{\rho_+} f^{**}(\rho_+) - f^{**}(\rho_+)$, and it is easily verified that the right-hand side always takes nonnegative values since it is an increasing function of ρ_+ vanishing for $\rho_+ = 0$.

Turning to a two-dimensional setup, we now consider an elementary cell $[0, L_*]^2$ with $L_* = 1$ or 2 nm and a circular inclusion carrying surface charges. The inclusion is positioned at the center of the elementary cell and has radius $0.3L_*$. The fluid domain Ω corresponds

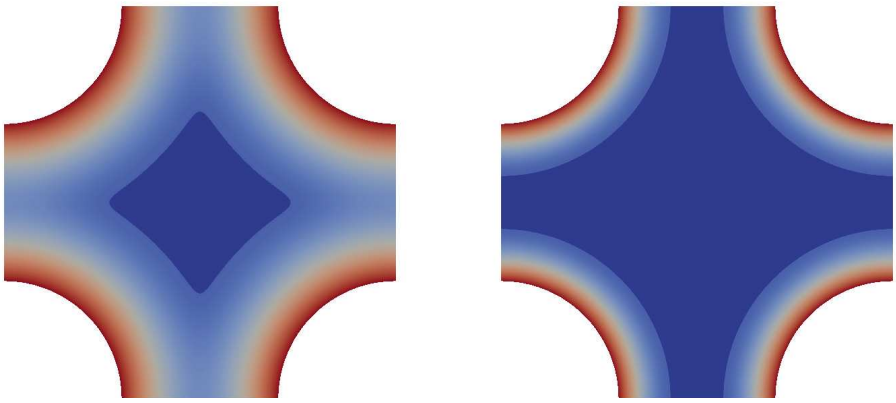

FIGURE 6. Circular inclusion within compensating trivalent counter-ion. Concentration profiles for $L_* = 1$ nm (left, values between 0.014 and 12.47 mol.L^{-1}) and $L_* = 2$ nm (right, values between 0.011 and 12.92 mol.L^{-1}). The two panels are rescaled to the same size.

to the elementary cell minus the circular inclusion. We set the surface charge density to $\Sigma_S = 0.5$ C.m^{-2} and consider dissolved counter-ions with valence $Z_+ = 3$ and diameter $\sigma = 4.5$ Å, yielding the canonical constraint $\rho_+^{\text{mean}} = 3.26$ mol.L^{-1} for $L_* = 1$ nm and $\rho_+^{\text{mean}} = 1.63$ mol.L^{-1} for $L_* = 2$ nm, while the reduced temperature T^* is equal to 0.0704 (below T^*_{crit}). Figure 6 presents concentration profiles for $L_* = 1$ nm (left panel) and $L_* = 2$ nm (right panel). The representation has been shifted using periodicity by half the length of the elementary cell in each direction to illustrate the fact that the dilute phase forms a droplet away from the charged circular inclusions for $L_* = 1$ nm. The conclusions drawn from the one-dimensional configuration carry over to the present two-dimensional configuration. The condensed phase screens out most of the surface charge carried by the circular inclusions. The predictions are in stark contrast with the PB theory, with substantial differences observed in the concentration profiles and, consequently, on the osmotic pressure.

5. Results with added salt

In this section, we consider ionic solutions with added salt. Implementing the numerical methodology described in Sect. 3 requires determining (or, at least, approximating with high accuracy) the convex hull of the bulk free energy density as a bivariate function of the counter- and co-ion densities. Within the RPM where the ions carry opposite charges, a simple approach can be devised based on a univariate function of the total ionic density only [50]. This is the case for symmetric electrolytes addressed in Sect. 5.1. In the more general case where the two charges are not opposite, a discrete double Legendre–Fenchel transform is employed [51]. This is the case for nonsymmetric electrolytes addressed in Sect. 5.2.

5.1. **Symmetric electrolytes.** In the case of symmetric electrolytes where $Z_+ + Z_- = 0$ (corresponding to the RPM), it is possible to write $f(\rho) = f_{\text{id}}(\rho) + f_{\text{corr}}(\rho_{\text{tot}})$ exploiting the fact that f_{corr} only depends on ρ_{tot}. Re-arranging the ideal part leads to

$$f(\rho) = f_{\text{tot}}(\rho_{\text{tot}}) + f_{\text{rel}}(\rho), \tag{26}$$

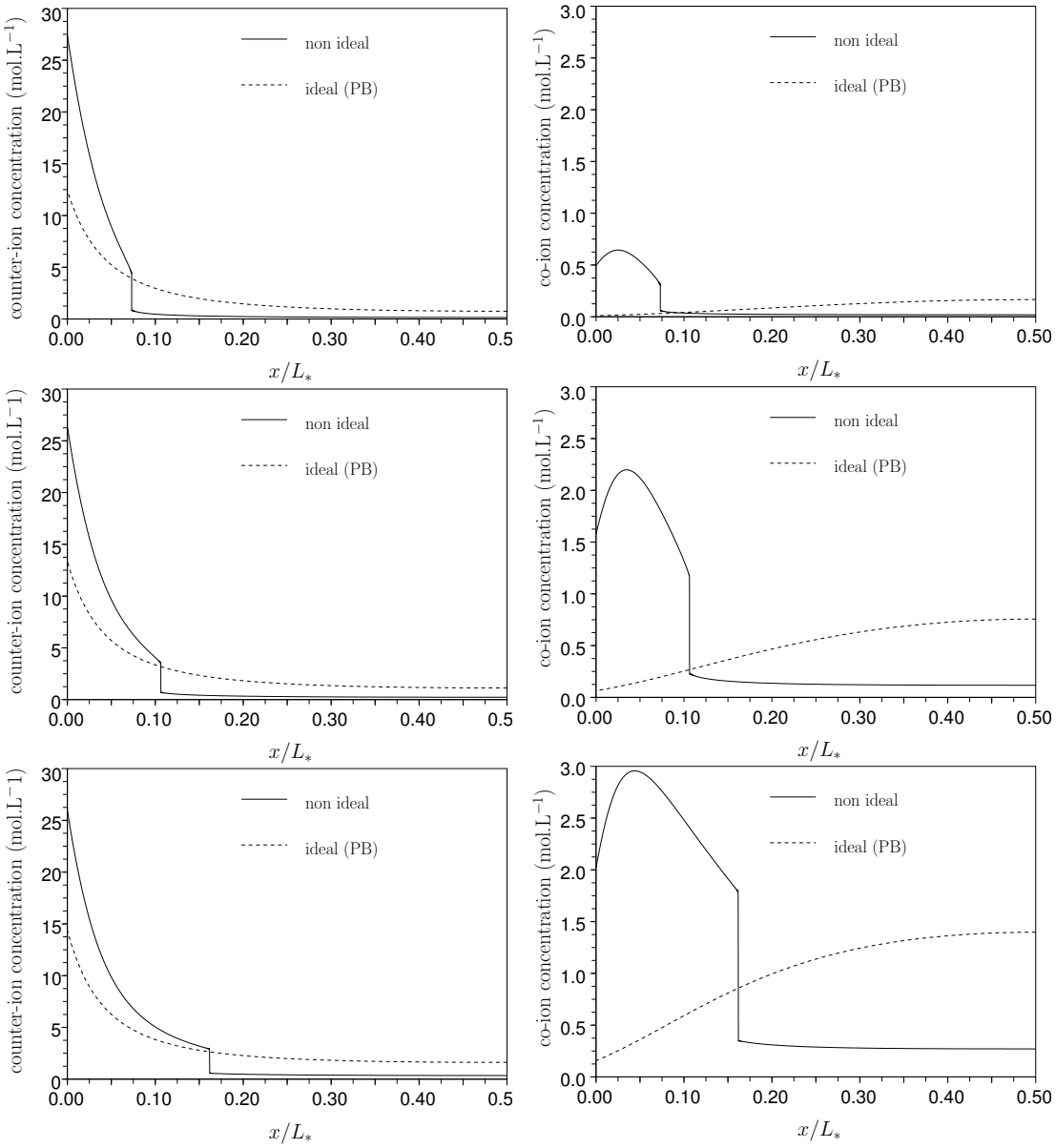

FIGURE 7. Double-layer configuration for a symmetric divalent electrolyte with $L_* = 1$ nm, $\Sigma_S = 0.2$ C.m^{-2}, and $\rho^{salt} = 0.1$ (top line), 0.5 (center line), and 1.0 mol.L^{-1} (bottom line). Concentration of counter-ions (left column) and co-ions (right column) as a function of the distance to the wall.

where

$$f_{tot}(\rho_{tot}) = \frac{1}{\beta\sigma^3}\hat{\rho}_{tot}(\log(\hat{\rho}_{tot}) - 1) + f_{corr}(\rho_{tot}), \tag{27}$$

and

$$f_{\rm rel}(\rho) = \frac{1}{\beta\sigma^3} \sum_{i=\pm} \hat{\rho}_i \log\left(\frac{\hat{\rho}_i}{\hat{\rho}_{\rm tot}}\right). \tag{28}$$

The bivariate function $f_{\rm rel}$ is convex in the ionic densities, while the convexity properties of the univariate function $f_{\rm tot}$ can be deduced from the phase diagram of Figure 2. Specifically, for a given reduced temperature T^* below the critical temperature $T^*_{\rm crit}$, the binodal points of $f_{\rm tot}$, denoted by $\hat{\rho}^\flat_{\rm tot}$ and $\hat{\rho}^\sharp_{\rm tot}$, are determined from the liquid-vapor coexistence curves of Figure 2. The subset $\mathcal{K}^{**}$ of the two-dimensional phase space then consists of two connected components (associated with the dilute and condensed phases) separated by the stripe $\{\hat{\rho}^\flat_{\rm tot} \leq \hat{\rho}_+ + \hat{\rho}_- \leq \hat{\rho}^\sharp_{\rm tot}\}$ whose boundary are two parallel lines in the (ρ_+, ρ_-)-plane.

We first consider the double-layer configuration with $L_* = 1$ nm, $\Sigma_{\rm S} = 0.2$ C.m^{-2}, valences $Z_+ = -Z_- = 2$, and diameter $\sigma = 2.2$ Å. This yields $\rho_+^{\Sigma_{\rm S}} = 2.076$ mol.L^{-1}, while $T^* = 0.07746$ (below $T^*_{\rm crit}$). We consider the values $\rho^{\rm salt} = 0.1$, 0.5 and 1.0 mol.L^{-1}. Counter- and co-ion concentration profiles are presented, respectively, in the left and right panels of Figure 7. Once again, predictions are in stark contrast with those obtained with the PB description. Interestingly, only one interface appears in the fluid domain Ω, and the condensed phase close to the charged wall contains most of the counter-ions, but also most of the co-ions. Spatial inhomogeneities are however present in the condensed phase. In particular, we observe that the co-ion concentration is non-monotone in the condensed phase. This phenomenon is explained by the Neumann boundary condition implicitly satisfied by the co-ion concentration and resulting from the constancy of the electro-chemical potential combined with the Neumann boundary condition on the electrostatic potential. Hence, even if most of the co-ions lie in the condensed phase, they are still somewhat repelled away from the wall by the negative surface charge. Finally, a comparison with the more elaborate approach of Sect. 5.2 (which also incurs numerical errors owing to discretization) to determine the subset $\mathcal{K}^{**}$ shows relative differences in predicted ionic densities below 10^{-4} away from the interface and 10^{-2} near the interface.

Figure 8 presents a different viewpoint, in that the cloud of points (ρ_+, ρ_-) is presented in the state space. Each point corresponds to the value obtained at a node of the finite element mesh. Results are presented for the case $L_* = 1$ nm considered above, and also for $L_* = 0.8$ nm and $L_* = 1.6$ nm. For fixed L_*, moving from right to left along a set of points corresponds to moving away from the charged wall. Interestingly, higher ionic concentrations are reached for larger values of L_*. Moreover, in Figure 8, the two parallel oblique lines indicate the boundary of the subset $\mathcal{K}^{**}$ in which the ionic densities are sought. Thus, the results show that the constraint that the ionic densities take values in the subset $\mathcal{K}^{**}$ is very well satisfied, up to very few mesh nodes (less than 0.1%).

Finally, Figure 9 presents counter- and co-ion isocontours for the configuration with circular inclusions with $L_* = 1$ nm, $\Sigma_{\rm S} = 0.2$ C.m^{-2}, and $\rho^{\rm salt} = 0.5$ mol.L^{-1}. We observe again the formation of a single interface whose shape closely follows that of the circular inclusion, and that the condensed phase contains most of the counter-ions and co-ions, the latter exhibiting a non-monotone behavior within this phase.

5.2. **Nonsymmetric electrolytes.** For nonsymmetric electrolytes where $Z_+ + Z_- \neq 0$, the convex hull of f can be evaluated numerically using a double discrete Legendre–Fenchel transform following the algorithm recently developed in [51] (where phase diagrams for various choices of $Z_\pm$ are presented). As discussed in Sect. 3.2, the chemical potentials used in the

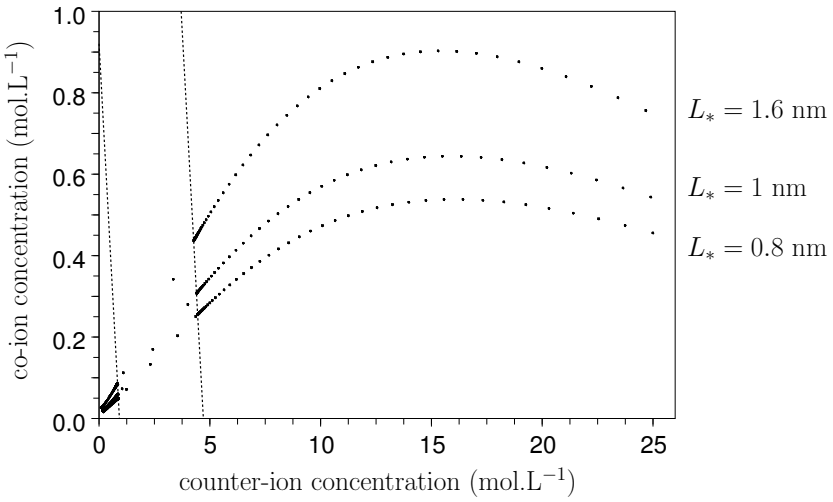

FIGURE 8. Double-layer configuration for a symmetric divalent electrolyte with $L_* = 0.8$, 1 and 1.6 nm, $\Sigma_S = 0.2$ C.m^{-2}, and $\rho^{\text{salt}} = 0.1$ mol.L^{-1}. Each point corresponds to ionic densities obtained at a certain node of the finite element mesh. The two parallel oblique lines indicate the boundary of the subset $\mathcal{K}^{**}$.

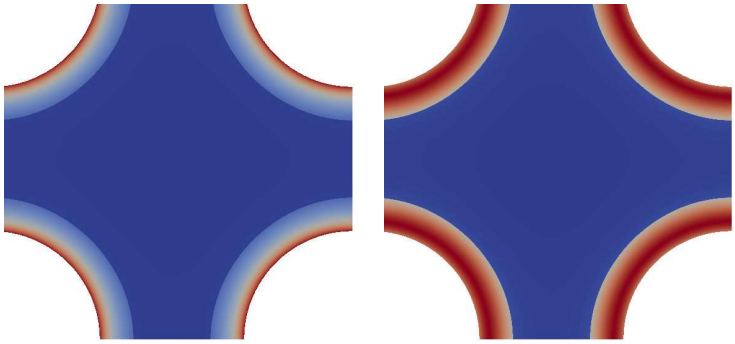

FIGURE 9. Circular inclusion within symmetric divalent electrolyte for $L_* = 1$ nm, $\Sigma_S = 0.2$ C.m^{-2}, and $\rho^{\text{salt}} = 0.5$ mol.L^{-1}. Concentration isocontours for counter-ions (left, values between 0.27 and 25.3 mol.L^{-1}) and co-ions (right, values between 0.09 and 1.82 mol.L^{-1}).

Newton–Raphson iterations are obtained from the partial derivatives of the convex hull of the bulk free energy density. To this purpose, values of the convex hull f^{**} and of its derivatives are tabulated on a fine grid of the phase space (ρ_+, ρ_-). When the function f^{**} is only known through tabulated values and not analytically, the sharp interface approximation with adaptively refined meshes becomes more delicate numerically. In our numerical experiments as $\eta \to 0^+$, we observed that ionic densities feature spurious oscillations in a tight vicinity of the interface whose measure tends to zero as $\eta \to 0^+$. Such oscillations concern less than 0.1% of the mesh nodes, and the corresponding values of ionic concentrations are omitted in the results presented below.

We focus on a nonsymmetric electrolyte with $Z_+ = 2$ and $Z_- = -1$, both ions having the same diameter $\sigma = 2.2$ Å. The reduced counter-ion temperature is set to $T_+^* = 0.07$ below the critical temperature $T_{\rm crit}^* = 0.0785$, while $T_-^* = 4T_+^*$ lies above this value. As a consequence, the function $\rho_+ \mapsto f(\rho_+, 0)$ is nonconvex, while the function $\rho_- \mapsto f(0, \rho_-)$ is convex. Therefore, the subset $\mathcal{K}^{**}$ has now a completely different shape than in the symmetric case; specifically, it intersects the ρ_+-axis, but not the ρ_--axis in the state space. Figure 10 presents the boundary of the subset $\mathcal{K}^{**}$ for the values $T_+^* = 0.05$, 0.06, 0.07 and 0.075. The lower the value of T_+^*, the larger the subset $\mathcal{K}^{**}$. In the four cases presented in Figure 10, the subset $\mathcal{K}^{**}$ does not intersect the ρ_--axis (it does so for reduced temperatures $T_+^* \leq 0.0785/4 \approx 0.0196$).

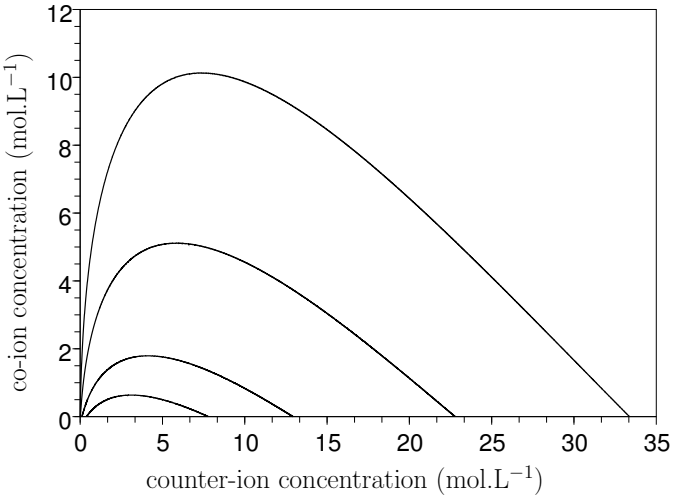

FIGURE 10. Phase separation diagram for a nonsymmetric 2:–1 electrolyte. Boundary of the subset $\mathcal{K}^{**}$ for the values $T_+^* = 0.05$, 0.06, 0.07 and 0.075; the lower the reduced temperature T_+^*, the larger the subset $\mathcal{K}^{**}$.

Counter- and co-ion concentration profiles are presented for the double-layer configuration with $L_* = 1$ nm, $\Sigma_{\rm S} = 0.1$ C.m^{-2} (yielding $\rho_+^{\Sigma_{\rm S}} = 1.04$ mol.L^{-1}), and $\rho^{\rm salt} = 0.1$ or 0.25 mol.L^{-1} in the left and right panels of Figure 11, respectively. The main result is, once again, the formation of an interface near the charged surface, with higher values for both counter- and co-ion densities. Interestingly, the ionic solution separates into two phases, with both counter- and co-ion densities jumping at the interface. Figure 12 presents the cloud of points (ρ_+, ρ_-) in the state space, each point corresponding to a node of the finite element mesh. For fixed $\rho^{\rm salt}$, moving from right to left along a set of points corresponds to moving away from the charged wall. The boundary of the subset $\mathcal{K}^{**}$ is indicated by the dotted line. Less than 0.1% of mesh nodes contribute to densities falling outside $\mathcal{K}^{**}$.

6. Conclusions

The main findings of the present study can be summarized as follows. The formation of a condensed layer near the charged surface screens out most of the surface charge (at least 90% of it in our experiments, with up to 99% in some cases). Density profiles are therefore in stark contrast with PB predictions. In particular, the total pressure, albeit slightly positive,

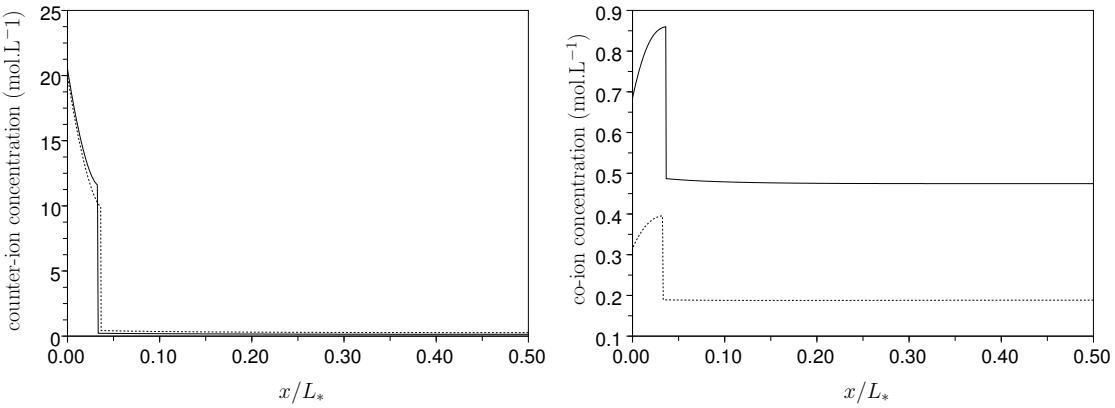

FIGURE 11. Double-layer configuration for a nonsymmetric 2:–1 electrolyte with $L_* = 1$ nm, $\Sigma_S = 0.1$ C.m^{-2}, and $\rho^{salt} = 0.1$ (dotted) or 0.25 mol.L^{-1} (solid). Concentration of counter-ions (left) and co-ions (right) as a function of the distance to the wall.

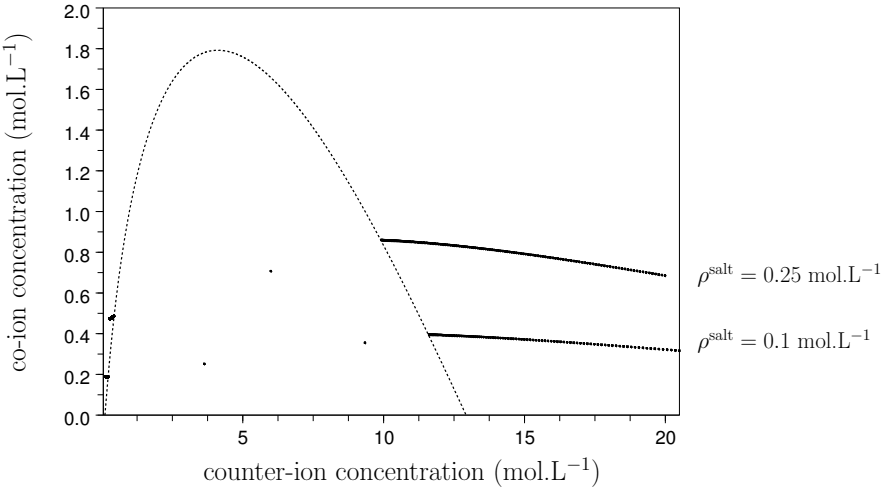

FIGURE 12. Double layer configuration for a nonsymmetric 2:–1 electrolyte with $L_* = 1$ nm, $\Sigma_S = 0.1$ C.m^{-2}, and $\rho^{salt} = 0.1$ and 0.25 mol.L^{-1}. Each point corresponds to ionic densities obtained at a certain node of the finite element mesh. The dotted line indicates the boundary of the subset $\mathcal{K}^{**}$.

is much smaller than the PB prediction. Moreover, for the periodic network of circular inclusions, the dilute phase can form a droplet away from the inclusions, while the condensed layer roughly follows the shape of the inclusions. In the case of ionic solutions with added salt, the appearance of a single interface is again observed in the fluid domain separating a condensed phase close to the charged surface and a dilute phase away from it. The condensed phase contains most of the counter-ions and again screens out most of the surface charge. The co-ion density is higher in the condensed phase than in the dilute phase. Moreover, the co-ion density is non-monotone within the condensed phase, as co-ions still tend to be repelled by the surface charges.

The present methodology, which is applicable to multi-dimensional geometries, can be of interest to study phase separation in confined ionic solutions in other applicative settings. As natural extensions of this work, one could now include the effect of non-ideality in multi-scale approaches which currently use the PB theory as a starting point [52, 53, 54, 55]. Another important issue is that of dynamical properties, in particular the coupling of ion dynamics with fluid flows resulting in the so-called electro-kinetic effects [56]. The present DFT formulation can be used to include non-ideality in numerical approaches which couple hydrodynamic flows to ionic fluxes via time-dependent DFT [57].

Acknowledgments

Partial support by ANDRA (French National Agency for the Management of Nuclear Waste) is gratefully acknowledged; in particular, the first author has been supported through a PhD fellowship by ANDRA.

References

[1] P. W. Debye and E. Hückel. The theory of electrolytes. I. lowering of freezing point and related phenomena. Phys. Z., 24:185, 1923.
[2] J. L. Lebowitz and E. Waisman. Mean spherical model integral equations for charged hard spheres. I. Method of solution. J. Chem. Phys., 56:3086–3093, 1972.
[3] J. L. Lebowitz and E. Waisman. Mean spherical model integral equations for charged hard spheres. II. Results. J. Chem. Phys., 56:3093–3099, 1972.
[4] L. Blum. Mean spherical model for asymmetric electrolytes. Mol. Phys., 30:1529–1535, 1975.
[5] L. Blum and J. S. Høye. Mean spherical model for asymmetric electrolytes. 2. Thermodynamic properties and the pair correlation function. J. Phys. Chem., 81:1311–1316, 1977.
[6] B. Groh, R. Evans, and S. Dietrich. Liquid-vapor interface of an ionic fluid. Phys. Rev. E., 57:6944–6954, 1998.
[7] N. K. Bjerrum. K. Dan. Vidensk. Selsk. Mat. Fys. Medd., 7:1, 1926.
[8] W. Ebeling and M. Grigo. Ann. Phys. (Leipzig), 37:21, 1980.
[9] W. Ebeling and M. Grigo. J. Sol. Chem., 11:151, 1982.
[10] M. Fisher and Y. Levin. Criticality in ionic fluids: Debye-Hückel theory, Bjerrum, and beyond. Phys. Rev. Lett., 71:3826, 1993.
[11] Y. Levin and M. Fisher. Criticality in the hard-sphere ionic fluid. Physica A, 225:164, 1996.
[12] J. Jiang, L. Blum, O. Bernard, J. M. Prausnitz, and S. I. Sandler. Criticality and phase behavior in the restricted-primitive model electrolyte: description of ion association. J. Chem. Phys., 116:7977, 2002.
[13] J. E. Flores-Mena, M. C. Barbosa, and Y. Levin. Criticality in confined ionic fluids. Phys. Rev. E, 63:066104, 2001.
[14] O. Pizio, A. Patrykiejew, and S. Sokolowski. Phase behavior of ionic fluids in slitlike pores: a density functional approach for the restricted primitive model. J. Chem. Phys., 121:11957, 2004.
[15] O. Pizio and S. Sokolowski. Phase behavior of the restricted primitive model of ionic fluids with association in slitlike pores. density-functional approach. J. Chem. Phys., 122:144707, 2005.
[16] M. Baus and J.-P. Hansen. Statistical mechanics of simple Coulomb systems. Phys. Rep., 59:1, 1980.
[17] M. Jardat, J.-F. Dufrèche, V. Marry, B. Rotenberg, and P. Turq. Salt exclusion in charged porous media: a coarse-graining strategy in the case of montmorillonite clays. Physical Chemistry Chemical Physics, 11(12):2023–2033, March 2009.
[18] L. Dresner and K. A. Kraus. Ion exclusion and salt filtering with porous ion-exchange materials. J. Phys. Chem., 67:990, 1963.
[19] L. Dresner. The exclusion of ions from charged microporous solids. J. Phys. Chem., 69:2230, 1965.
[20] S. Engström and H. Wennerström. Ion condensation on planar surfaces. a solution of the Poisson-Boltzmann equation for two parallel charged plates. J. Phys. Chem., 82:2711, 1978.
[21] E. Trizac, L. Bocquet, M. Aubouy, and H. H. von Grünberg. Alexander's prescription for colloidal charge renormalization. Langmuir, 19:4027–4033, 2003.

[22] P. Attard, D. J. Mitchell, and B. W. Ninham. Beyond Poisson-Boltzmann: images and correlations in the electrical double-layer. I Counterions only. J. Chem. Phys., 88:4987, 1988.
[23] R. Kjellander, S. Marcelja, and J. P. Quirk. Attractive double-layer interactions between calcium clay particles. Journal of Colloid and Interface Science, 126(1):194–211, November 1988.
[24] R. Kjellander, S. Marcelja, R. M. Pashley, and J. P. Quirk. Double-layer ion correlation forces restrict calcium-clay swelling. The Journal of Physical Chemistry, 92(23):6489–6492, November 1988.
[25] A. G. Moreira and R. R. Netz. Binding of similarly charged plates with counterions only. Phys. Rev. Lett., 87:078301, 2001.
[26] R. R. Netz. Electrostatistics of counter-ions at and between planar charged walls: From Poisson-Boltzmann to the strong-coupling theory. Eur. Phys. J. E, 5:557, 2001.
[27] A. Yu. Grosberg, T. T. Nguyen, and B. I. Shklovskii. The physics of charge inversion in chemical and biological systems. Rev. Mod. Phys., 74:329, 2002.
[28] L. Samaj and E. Trizac. Counterions at highly charged interfaces: From one plate to like-charge attraction. Phys. Rev. Lett., 106, 2011.
[29] F. Paillusson and E. Trizac. Interaction regimes for oppositely charged plates with multivalent counterions. Physical Review E, 84(1):011407, July 2011.
[30] V. Kralj-Iglic and A. Iglic. A simple statistical mechanical approach to the free energy of the electric double layer including the excluded volume effect. J. Phys. II (France), 6:477–491, 1996.
[31] J.-P. Hansen, D. Goulding, and R. van Roij. Effective interactions between charged colloidal particles : Repulsion, attraction and phase separation. J. Phys. IV (France), 10:5, 1997.
[32] R. R. Netz and H. Orland. Field theory for charged fluids and colloids. Europhys. Lett., 45:726, 1999.
[33] J.-P. Hansen and H. Löwen. Effective interactions between electric double-layers. Annu. Rev. Phys. Chem., 51:209–242, 2000.
[34] D. Gillespie, W. Nonner, and R. S. Eisenberg. Density functional theory of charged, hard-sphere fluids. Phys. Rev. E., 68:2003, 031503.
[35] L. Mier-y Teran, S. H. Suh, H .S White, and H. T. Davis. A nonlocal free energy density functional approximation for the electrical double layer. J. Chem. Phys., 92:5087, 1990.
[36] H. Löwen, J.-P. Hansen, and P. A. Madden. Nonlinear counterion screening in colloidal suspensions. J. Chem. Phys., 98:3275–3289, 1993.
[37] A. Oleksy and J.-P. Hansen. Wetting and drying scenarios of ionic solutions. Mol. Phys., 109(7-10):1275–1288, 2011.
[38] H. Greberg, R. Kjellander, and T. Akesson. Ion-ion correlations in electric double layers from monte carlo simulations and integral equation calculations. Molecular Physics, 87(2):407–422, 1996.
[39] H. Greberg, R. Kjellander, and T. Akesson. Ion-ion correlations in electric double layers from monte carlo simulations and integral equation calculations part 2. case of added salt. Molecular Physics, 92(1):35–48, 1997.
[40] A. Delville and R. J. M. Pellenq. Electrostatic attraction and/or repulsion between charged colloids: A (NVT) monte-carlo study. Molecular Simulation, 24(1-3):1–24, 2000.
[41] Roland Kjellander, Alexander P. Lyubartsev, and Stjepan Marcelja. McMillan-Mayer theory for solvent effects in inhomogeneous systems: Calculation of interaction pressure in aqueous electrical double layers. The Journal of Chemical Physics, 114(21):9565–9577, June 2001.
[42] R. J. M. Pellenq. On the origin of cement cohesion. Actualite Chimique, pages 12–22, March 2004. WOS:000220862400003.
[43] W. Kohn and L. J. Sham. Self-consistent equations including exchange and correlation effects. Phys. Rev., 140:A1133–A1138, 1965.
[44] A. Ern, R. Joubaud, and T. Lelièvre. Mathematical study of non-ideal electrostatic correlations in equilibrium electrolytes. Nonlinearity, 25:1635–1652, 2012.
[45] L. Modica. The gradient theory of phase transitions and the minimal interfaee criterion. Arch. Ration. Mech. Anal, 98:123–142, 1987.
[46] Andrea Braides. Γ-convergence for Beginners. Oxford lecture series in mathematics, 2002.
[47] C.B. Muratov. Droplet phases in non-local Ginzburg-Landau models with Coulomb repulsion in two dimensions. Comm. Math. Phys., 299:45–87, 2010.
[48] R. Choksi and P. Sternberg. Periodic phase separation: the periodic isoperimetric and Cahn-Hilliard problems. Interfaces and Free Boundaries, 8:371–392, 2006.

[49] D. Goldman, C. Muratov, and S. Serfaty. The Gamma-limit of the two-dimensional Ohta-Kawasaki energy. I. Droplet density. arXiv:1201.0222, 2012.
[50] R. Joubaud. Modélisation mathématique et numérique des fluides à l'échelle nanométrique. PhD thesis, University Paris-Est, 2012.
[51] L. Contento, A. Ern, and R. Vermiglio. An efficient algorithm for the double Legendre–Fenchel transform with application to phase separation. Technical report, University Paris-Est, CERMICS, 2013.
[52] C. Moyne and M. A. Murad. A two-scale model for coupled electro-chemo-mechanical phenomena and onsager's reciprocity relations in expansive clays: I homogenization analysis. Transport in Porous Media, 62(3):333–380, March 2006.
[53] C. Moyne and M. A. Murad. A two-scale model for coupled electro-chemo-mechanical phenomena and onsager's reciprocity relations in expansive clays: II computational validation. Transport in Porous Media, 63(1):13–56, April 2006.
[54] G. Allaire, A. Mikelić, and A. Piatnitski. Homogenization of the linearized ionic transport equations in rigid periodic porous media. J. Math. Phys., 51:123103, 2010.
[55] G. Allaire, R. Brizzi, J-F Dufrêche, A. Mikelić, and A. Piatnitski. Role of non-ideality for the ion transport in porous media: derivation of the macroscopic equations using upscaling. in preparation, 2012.
[56] I. Pagonabarraga, B. Rotenberg, and D. Frenkel. Recent advances in the modelling and simulation of electrokinetic effects: bridging the gap between atomistic and macroscopic descriptions. Phys. Chem. Chem. Phys., 12(33):9566–9580, 2010.
[57] B. Rotenberg, I. Pagonabarraga, and D. Frenkel. Coarse-grained simulations of charge, current and flow in heterogeneous media. Faraday Discussions, 144(0):223–243, October 2009.

1: ANDRA, DRD/EAP, Parc de la croix blanche, 1,7 rue Jean Monnet, 92298 Châtenay-Malabry Cedex

2: University Paris-Est, CERMICS, Ecole des Ponts ParisTech, 77455 Marne la Vallée cedex 2, France

3: Department of Mathematics, Imperial College London, SW7 2AZ London, UK

4: CNRS, UMR 7195 PECSA, 75005 Paris, France

5: UPMC Univ. Paris 06, UMR 7195 PECSA, 75005 Paris, France

6: Department of Mathematics and Computer Science, University of Udine, Italy